

# Simulation analysis with “rock” muons from atmospheric neutrino interactions in the ICAL detector at INO

R. Kanishka<sup>\*,#,⊕</sup>, D. Indumathi<sup>†,⊕</sup>, V. Bhatnagar<sup>‡</sup>

<sup>#</sup>*ANPD, Saha Institute of Nuclear Physics, 1/AF Saltlake, Kolkata 700064, India,*

<sup>⊕</sup>*Homi Bhabha National Institute, Mumbai 400094, India.*

<sup>†</sup>*The Institute of Mathematical Sciences, Chennai 600113, India,*

<sup>‡</sup>*Physics Department, Panjab University, Chandigarh 160014, India*

July 19, 2022

**Abstract** : The proposed magnetised Iron CALorimeter detector (ICAL) to be built in the India-based Neutrino Observatory (INO) laboratory aims to study atmospheric neutrinos and its properties such as precision measurements of oscillation parameters and the neutrino mass hierarchy. High energy charged current (CC) interactions of atmospheric neutrinos with the rock surrounding the detector produce so-called “rock muons” along with hadrons. While the hadron component of these events are absorbed in the rock itself, the rock muons traverse the rock and are detected in the detector. These rock muon events can be distinguished from cosmic muons only in the upward direction and can provide an independent measurement of the oscillation parameters. A simulation study of these events at the ICAL detector shows that, although reduced in significance compared to muons produced in direct CC neutrino interactions with the detector, these events are indeed sensitive to the oscillation parameters, achieving a possible  $1\sigma$  precision of 10% and 27% in determining  $|\Delta m_{32}^2|$  and  $\sin^2 \theta_{23}$ , respectively.

## 1 Introduction

Neutrinos as described by the “Standard Model” are massless and occur in three distinct flavours  $\nu_e, \nu_\mu, \nu_\tau$ . Many experiments on solar [1]–[10], atmospheric [11]–[19], accelerator [20] and reactor [21] neutrinos have confirmed that neutrinos have mass, and the flavour states are mixtures of mass eigenstates ( $\nu_1, \nu_2, \nu_3$ ) with different masses—this leads to the phenomenon of neutrino

---

\*Email: kanishka.rawat.phy@gmail.com; indu@imsc.res.in; vipin@pu.ac.in

oscillations and is an important piece of evidence for physics beyond the Standard Model. The PMNS neutrino mixing matrix [22, 23], can be parametrized in terms of three mixing angles and a charge conjugation-parity violating (CP) phase  $\delta_{CP}$ . Some recent results from reactor neutrino experiments [24, 25] have reconfirmed the oscillations in the neutrino flavours and non-zero value of the across-generation mixing angle  $\theta_{13}$ . Apart from this, these experiments determine the extent of mixing and the differences between the squared masses as well, although not the absolute values of the masses themselves.

There are three possible arrangements of the neutrino masses. For normal ordering, we have<sup>1</sup>  $m_1 < m_2 \ll m_3$ ; hence,  $\Delta m_{32}^2 \equiv m_3^2 - m_2^2 > 0 \text{ eV}^2$  and  $m_3 \gtrsim \sqrt{\Delta m_{32}^2} \simeq 0.03\text{--}0.07 \text{ eV}$ . For inverted ordering,  $m_2 \gtrsim m_1 \gg m_3$  with  $m_{1,2} \gtrsim \sqrt{\Delta m_{23}^2} \simeq 0.03\text{--}0.07 \text{ eV}$ ; hence,  $\Delta m_{32}^2 \equiv m_3^2 - m_2^2 < 0 \text{ eV}^2$ . In the degenerate case,  $m_1 \simeq m_2 \simeq m_3$ . If the ordering is strong, then the ordering also determines the mass hierarchy; this problem [26] is still not solved and it is believed that upcoming experiments like the magnetised Iron Calorimeter detector (ICAL) at the proposed India-based Neutrino Observatory (INO) [27] will be able to answer this problem along with the precision determination of oscillation parameters. Note that the sign of  $\Delta m_{32}^2$  (or, equivalently, the sign of  $\Delta m_{31}^2$ ) which determines the mass ordering is still unknown, as well as the octant of  $\theta_{23}$ . Precision experiments sensitive to matter effects during propagation of the neutrinos through the Earth can determine the sign of  $\Delta m_{31}^2$ . Another open question regarding the neutrinos is, whether there is CP violation in the leptonic sector. Experiments such as DUNE and JUNO [28, 29] will also be sensitive to the currently unknown oscillation parameters such as the mass hierarchy and the CP phase.

The ICAL detector at the proposed INO lab will be a 51 kton magnetised iron detector with layers of iron of 56 mm thickness interspersed with active RPC detectors in the 40 mm air gap. It will be optimised to study muons produced in the charged-current (CC) interactions of atmospheric neutrinos with the detector. Hence it is also suitable for measuring the so-called upward-going muon flux due to CC interactions of the atmospheric neutrinos with the rock surrounding the detector (the downward-going muon flux is swamped by the cosmic ray muon background and is therefore not useful for neutrino oscillation studies). The muon loses an unknown fraction of its energy while traversing the rock to reach the detector, it still carries an imprint of the oscillations of the parent neutrino that produced it. It is therefore useful to study these upward-going or rock muons that have a characteristic signature in the detector. In this paper, we discuss the simulations studies in the ICAL detector at INO using upward-going muons and their significance. This study allows us an independent measurement of oscillation parameters.

The paper is organized as follows. In section 2, we briefly discuss the upward-going muons at the ICAL detector. In section 3, we discuss the detector response for such muons. In section 4 the detailed simulation procedure including data generation, methodology for oscillation studies and  $\chi^2$  analysis are described. In section 5, we discuss the results: sensitivity to measurements of the oscillation parameters, and comparison of ICAL sensitivity with existing data [30]. We conclude with discussions in section 6.

---

<sup>1</sup>We have used natural units with  $\hbar = c = 1$ .

## 2 Upward-going Muons at ICAL Detector

The ICAL detector will be located under 1279 m (approx) high mountain peak and will have a minimum rock cover of about 1 km in all directions, thereby reducing the cosmic muon backgrounds [31]. Upward-going muons arise from the interactions of atmospheric neutrinos with the rock material surrounding the detector, typically within the range of  $\sim 200$  m (beyond this distance, the muon energy loss is so large that only very high energy muons can reach the detector, but the flux of such events is very small). These upward-going muons, also known as rock muons [32, 33, 34] can provide an independent measurement of the oscillation parameters, although the sensitivity of upward-going muons to the oscillation parameters is lower than contained-vertex muons produced by  $\nu_\mu$  interactions inside ICAL. But an independent measurement using upward-going muons will provide a consistency check with the contained vertex analysis, that would result in slight improvement of the overall measurement. This kind of analysis is helpful in any neutrino experiment.

Fig. 1 shows a schematic of the processes that give rise to upward-going muons at the ICAL detector. Neutrinos, after interacting with rock, produce hadrons and muons. The hadrons get absorbed in the rock and the upward-going muons travel a distance  $L$  making an angle  $\theta$  with the  $z$ -axis (where  $\theta = 0$  is the upward-direction w.r.t. ICAL), and finally reach the ICAL detector. Due to the kinematics, especially at higher neutrino energies, upward-going neutrinos also (dominantly) produce upward-going muons.

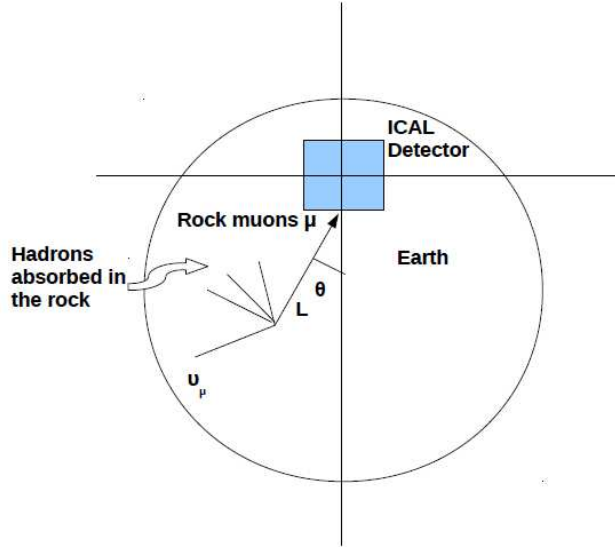


Fig. 1: Schematic (not to scale) of the processes that give rise to upward-going muons at ICAL.

Upward-going muons are to be discriminated from two other types of events. First, are those neutrino events that produce muons through interactions inside the ICAL detector and are a part of the main studies of ICAL. This background can be eliminated by considering only those muon tracks that come from outside the ICAL detector, i.e., their tracks start at the edges of

ICAL and outside the fiducial volume. Secondly, cosmic ray muon events produced in the Earth's atmosphere directly leave tracks in ICAL detector. These form the main background in ICAL detector and can be eliminated by imposing an angle cut that allows only upward-going muons for the analysis since there are no cosmic ray muons arriving from below.

The muon loses a substantial part of its energy (on the average) in the rock before it reaches the detector so the oscillation signature becomes more complicated. The formula for the average muon energy loss for muons of energy  $E_\mu$  produced in the rock is given by [35]

$$\frac{dE_\mu}{dx} = -a - bE_\mu , \quad (1)$$

so the energy loss of the muons after propagation through a distance  $X$  g/cm<sup>2</sup> is:

$$E_\mu = (E_\mu^0 + \epsilon) \exp(-bX) - \epsilon , \quad (2)$$

where  $\epsilon = a/b$ ,  $E_\mu^0$  is the initial muon energy,  $a$  accounts for ionization losses and  $b$  accounts for the three radiation processes: bremsstrahlung, photoproduction and production of electron-positron pairs. We have  $\epsilon = a/b \sim 500$  GeV, where both  $a$  and  $b$  depend on  $E_\mu$ . This formula is approximate and indicative of the kind of energy loss at different energies. The actual upward-going muons have been simulated using the NUANCE neutrino generator [36] which takes into consideration the energy dependence of  $a$  and  $b$  as well as accounts for fluctuations.

Fig. 2 shows the energy  $E_\mu^{(obs)}$  of muons arriving at the detector from all possible upward directions as calculated from Eq. 2 versus the energy  $E_\mu^{(nuance)}$  obtained from NUANCE for a sample atmospheric neutrino flux with 10 years exposure at ICAL.

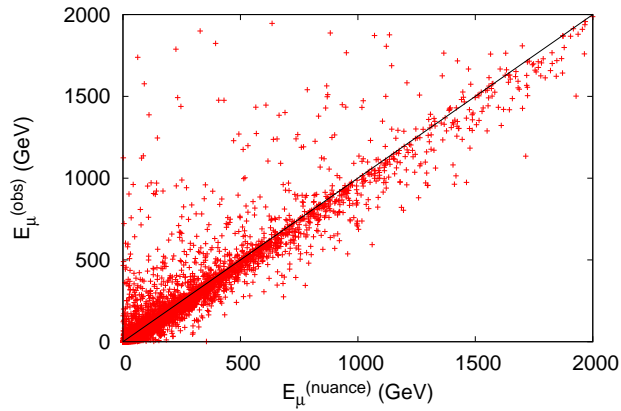


Fig. 2: Comparison of the energy  $E_\mu^{(obs)}$  of upward-going muons calculated from Eq. 2 vs.  $E_\mu^{(nuance)}$  as calculated by the NUANCE neutrino generator including fluctuations.

The dependence is linear on the average, with large fluctuations, especially at lower energies which are of interest for atmospheric neutrino studies. The energy loss depends on the distance  $L$  traversed through the rock of density  $\rho(L)$  from the production point to the detector,  $X = L\rho(L)$ , where  $L$  is determined from the polar angle  $\theta$  through

$$L = \sqrt{(R + L_0)^2 - (R \sin \theta)^2} + R \cos \theta , \quad (3)$$

where  $\cos \theta = 1$  corresponds to rock muons, where  $L_0 \sim 15 + 1$  km is the average height above the detector (assuming the atmospheric neutrinos are produced at 15 km above the surface of the Earth, and taking the detector to be 1 km underground) while  $R$  is the radius of the Earth.

A substantial number of muons are absorbed before they reach the detector. Though the observed number is small, they carry important signature of oscillation. The muon survival probability  $P_{\mu\mu}$  (which goes to 1 as  $E_\nu$  increases) in vacuum is given by

$$P_{\mu\mu} = 1 - \sin^2 2\theta_{23} \sin^2 \frac{1.27 \Delta m_{32}^2 L}{E}, \quad (4)$$

whereas the survival probability  $P_{\mu\mu}^m$  in matter can be approximated by [37]:

$$P_{\mu\mu}^m \approx 1 - \sin^2 2\theta_{23} [\sin^2 \theta_{13}^m \sin^2 \Delta m_{21,m}^2 + \cos^2 \theta_{13}^m \sin^2 \Delta m_{32,m}^2] - \sin^4 \theta_{23} \sin^2 2\theta_{13}^m \sin^2 \Delta m_{31,m}^2, \quad (5)$$

$$\equiv P_{\mu\mu}^{(2)} - \sin^2 \theta_{13} \times \left[ \frac{A}{\Delta - A} T_1 + \left( \frac{\Delta}{\Delta - A} \right)^2 (T_2 \sin^2[(\Delta - A)x] + T_3) \right]. \quad (6)$$

Here  $P_{\mu\mu}^{(2)}$  is the (2-flavour) matter-independent survival probability and the matter term is given by  $A = 7.6 \times 10^{-5} \rho$  (gm/cm<sup>3</sup>) $E$  (GeV). Here  $\Delta m_{ij}^2 \equiv (m_i^2 - m_j^2)$  and  $\Delta m_{ij,m}^2$  refer to the mass squared differences in matter. We have denoted the dependence on the dominant mass squared difference as  $\Delta$ :  $\Delta \sim \Delta m_{32}^2 \sim \Delta m_{31}^2$ , and in the last line  $T_{1,2,3}$  are coefficients independent of  $\Delta$ ; see Ref. [37, 38] for details. Using this, from the last line in Eq. (6), we see that, since  $A$  is positive for  $\nu$  and negative for  $\bar{\nu}$ ; hence  $P_{\mu\mu}$  is sensitive to the sign of the 2–3 mass squared difference via  $(A - \Delta)$ , or the neutrino mass ordering. A similar dependence has been seen in the oscillation probability  $P_{e\mu}$  as well. Note that the above expressions were given in order to clarify the dependences on the various oscillation parameters; precise numerical computations for the oscillation probabilities are used in the results section.

Before we study upward-going muons for their sensitivity to neutrino oscillations, we present some details on the detector resolution simulation studies.

### 3 Detector Response for Muons

The proposed magnetised ICAL detector at INO with 1.3–1.5 Tesla magnetic field will be capable of distinguishing  $\mu^+$  and  $\mu^-$  which arise from CC interactions of  $\bar{\nu}_\mu$  and  $\nu_\mu$  respectively. The ICAL detector consists of three identical modules of dimension 16 m  $\times$  16 m  $\times$  14.45 m. Each module consists of 151 alternate layers of 5.6 cm thick iron plates sandwiched between glass Resistive Plate Chambers (RPCs) [39], having total mass of about 51 kton. The iron plates act as the target for neutrino interactions to occur whereas RPCs are the active detector elements giving the trajectory of muons and hadrons [40] passing through them. The magnetic field is generated by passing current through copper coils, which pass through coil slots in the plates as shown in Fig. 3.

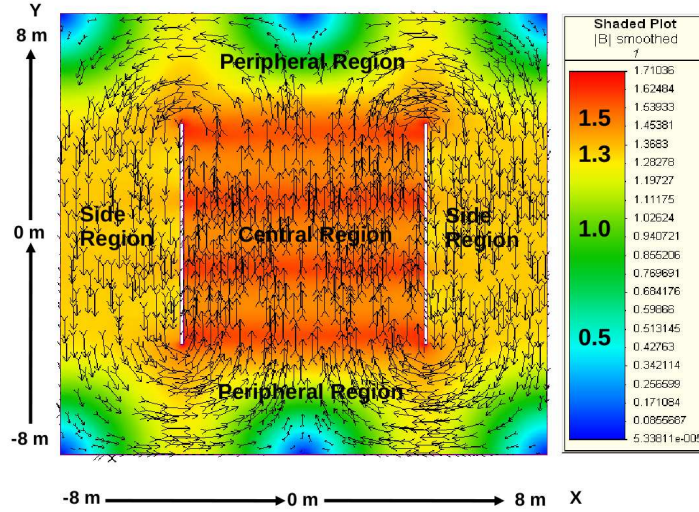


Fig. 3: Magnetic field map as generated by the MAGNET6 software in the central iron layer of the central module [41]; the gaps correspond to the slots for the copper coils to pass through.

The magnetic field is distributed in such a way that it divides the whole ICAL into three regions. The main region is the “central region” [42] within the coils slots which has the highest, as well as most uniform magnetic field in the  $y$  direction, while the magnetic field in the “side region” (outside the coil slots in the  $x$  direction) is about 15% smaller and in the opposite direction. The region labelled as “peripheral region” [43] (outside the central region in the  $y$  direction) has the most varying magnetic field in both magnitude and direction. Hence the side and peripheral regions will be affected by having a more complicated magnetic field as well as having edge effects i.e., both of them have a larger fraction of partially contained events (about 23% compared to 12% of events with vertex in the central region) where only a part of the muon trajectory/track is contained and detected within the detector.

As has been discussed in Refs. [42, 43], ICAL has good energy and direction resolution in both the central and peripheral regions of the detector. However, these studies on muon energy, direction reconstruction and charge identification capability were performed with a view to understand the detector response for the main events at ICAL, viz., CC muon neutrino interactions inside ICAL. Hence, all these studies used a simulated data sample where the neutrino interactions occurred *inside* ICAL so that the produced muons were also inside the detector.

For the current study, we need to understand the response of ICAL to muons that are entering the detector *from outside*. These are also very “clean” events in that there are no accompanying hadrons. Hence we first calibrated the detector response to such events. Note that the upward-going muons enter the detector through five different faces (left, right, front, back and bottom). While about half the upward-going muons have their vertices in the bottom of the detector, the four sides (left, right, front and back) of ICAL together account for the other half of the events. In each case, the muon experiences a different local magnetic field. Hence the response will be different in each case. However, muons that enter through the bottom face of the detector



experience regions corresponding to all the possible choices—central, peripheral and side. Hence, we study the response of the bottom face of the whole ICAL to muons. This contains portions of the “central” and “peripheral” regions and so its response is likely to be intermediate between the two.

As the muon enters ICAL, it produces signals in the RPCs. These signals are localised to a size of 3 cm, which determines the spatial resolution of the muon track in the  $x$ - and  $y$ -directions and are called “hits”. An event has hits in several layers (along the  $z$ -direction). Since the detection efficiency of the RPCs is 95%, there may be different numbers of  $x$ - and  $y$ -hits in any layer. Hence the total hits  $N_{hits}$  per event are then determined as the sum of the maximum value of the  $x$ - or  $y$ -hits for each layer.

The selection criteria to choose or drop an event were decided so as to get reasonable fits and hence resolutions. Mainly, one major selection criterion has been applied in the region to remove low energy tails; this was similar to that used in studying the peripheral muons [43]. The events were selected in a manner such that, if the track was fully contained (most likely scenario at lower energies) then it was considered for analysis, but if it was partially contained (more likely at higher energies), then the event was selected only if  $N_{hits} > 15$ . A somewhat looser constraint has been obtained by also taking into account the angle at which the muon enters (since the number of layers traversed and hence the number of hits in a track are dependent on this) by demanding that  $N_{hits}/\cos\theta > 15$ . This criterion removed muons that exited the detector leaving very short tracks inside, which were typically reconstructed with much smaller momenta than the true values.

This can be seen from Fig. 4 which explains the effect of the selection criterion on reconstructed momentum ( $P_{rec}$ ) in the region. Here, 10,000 muons with fixed input momenta and direction ( $\cos\theta$ ) were randomly generated with vertices uniformly distributed on the bottom face of ICAL, with uniform random azimuthal angle,  $0 < \phi < 2\pi$ . It can be seen that, at lower energy ( $P_{in} = 5$  GeV/c), the  $N_{hits}$  criterion does not significantly affect the momentum distribution as most of the events are fully contained. On the other hand, the hump at lower energy for  $P_{in} = 15$  GeV/c is due to the charge mis-identification which has been eliminated with the  $N_{hits}$  cut. (In fact, the condition that only one track be reconstructed, as demanded in the peripheral muon analysis [43], was not required as the present constraint on  $N_{hits}$  was found to be sufficient). The histogram was fitted with a Gaussian distribution to determine its width  $\sigma$ , from which the muon momentum resolution has been defined as the ratio  $\sigma/P_{in}$ , of the width to the initial momentum.

### 3.1 Reconstruction Efficiency and Resolution of Muons

Now we discuss the results on reconstruction efficiencies and energy and angular resolutions for the muons based on the selection criteria discussed earlier. Fig. 5 shows the reconstruction and charge identification efficiencies in the bottom region of ICAL.

The reconstruction efficiency, which is defined as the ratio of the number of reconstructed events to the total events simulated, has been found to be greater than 85% for energies less than 50 GeV and for angles greater than  $\cos\theta > 0.35$ . The relative charge identification (cid) efficiency, which is the ratio of the number of events with correctly identified muon charge sign to the total number of reconstructed events, is better than 95%, and in fact nearly 97% for  $p_\mu < 20$

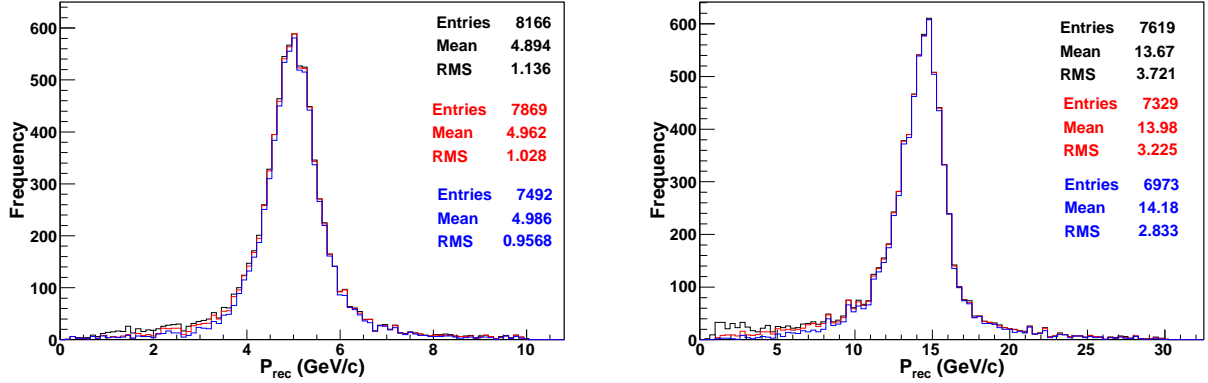


Fig. 4: The reconstructed momenta  $P_{rec}$  using selection criteria  $N_{hits} > n_0$  for partially contained events in the bottom region of ICAL at  $(P_{in}, \cos\theta) = (5 \text{ GeV/c}, 0.65)$  (left) and  $(P_{in}, \cos\theta) = (15 \text{ GeV/c}, 0.65)$  (right). In both figures, the black curve is without constraints on  $N_{hits}$ , red is with  $N_{hits}/\cos\theta > n_0$  and blue is for  $N_{hits} > n_0$ ;  $n_0 = 15$ .

GeV; it is better than 85% for  $E_\mu$  upto 150 GeV and  $\cos\theta > 0.35$ .

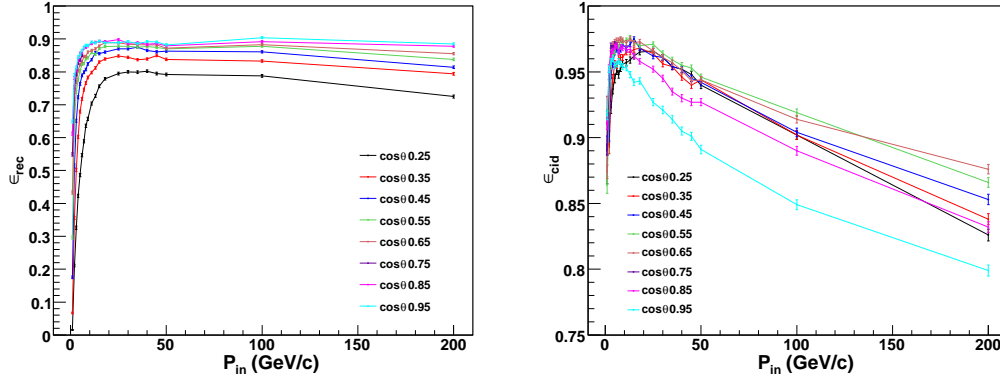


Fig. 5: The reconstruction efficiency (left) averaged over  $\phi$  for  $N_{hits}/\cos\theta > 15$ , as a function of  $P_{in}$  for different polar angles,  $\cos\theta = 0.25, \dots, 0.95$ . The charge identification efficiency (right) averaged over  $\phi$ . (Note that the  $y$ -axes scales are different.)

Fig. 6 shows the momentum resolution  $\sigma/P_{in}$  and the polar angle  $\theta$  resolution. Note that the polar angle resolution is the value of the width  $\sigma$  of the fitted gaussian in radians.

The muon resolutions are better than about 20% for muon energies less than 50 GeV and for angles greater than  $\cos\theta > 0.35$ , and worsen for larger energies and angles but remain less than 50% upto  $E_\mu < 150 \text{ GeV}$ . The  $\theta$  resolution, which was about a degree for few GeV region, is similar to that obtained from earlier studies [43]. We shall use these values of muon reconstruction efficiency and resolution in our simulations studies of upward-going muons in the next sections.



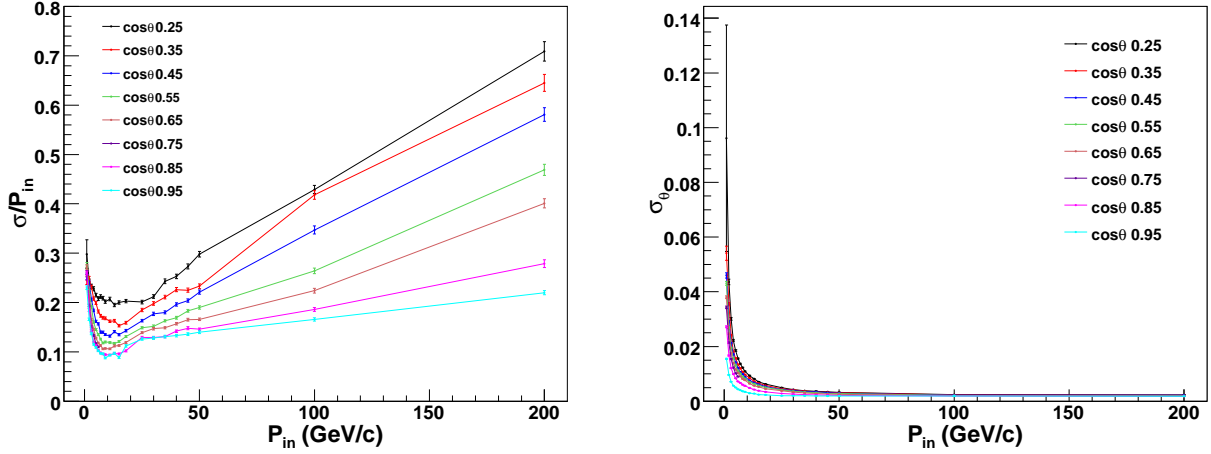


Fig. 6: Muon resolution (left) as a function of input momentum  $P_{in}$  and  $\cos \theta$ , averaged over  $\phi$ , for  $N_{hits}/\cos \theta > 15$ . The angular  $\theta$  resolution (right) is shown as a function of the input momentum  $P_{in}$  and  $\cos \theta$  in radians. (Note that the  $y$ -axes scales are different.)

## 4 Physics Analysis of Upward-going Muons

### 4.1 Event Generation

We have used the neutrino event generator NUANCE (version 3.5) [36] to generate events corresponding to an exposure of  $51 \text{ kt} \times 200 \text{ years}$  (that is, 200 years' at ICAL) of unoscillated upward-going muons in the energy range 0.8–200 GeV. The atmospheric neutrino fluxes provided by Honda et al. [44] at the Super Kamiokande experiment [45] were used. The ICAL detector specifications were defined inside NUANCE. Dimensions of the detector were chosen such that no events were generated inside the detector i.e., only its external geometry was used. The actual material in which interactions occurs is rock, whose density was taken to be  $2.65 \text{ gm/cm}^3$ . To cut off cosmic ray backgrounds, a cut on angle (optimized),  $0^\circ < \theta < 81^\circ$  ( $\cos \theta > 0.156$ ), was applied [46]. The NUANCE generator itself propagated the muon produced in the CC interaction to the closest surface of the ICAL detector by using appropriate energy loss formulae as discussed earlier.

Two data sets were generated: set I with “normal” fluxes, and set II with “swapped” fluxes where the muon and electron neutrino fluxes were interchanged. This was used to enable incorporation of oscillations later. Note that the energy and direction of the neutrino initiating the event is also available in NUANCE. These values are required to generate the correct neutrino oscillation and survival probabilities.

The number of muon events from these two channels are given by,

$$\begin{aligned} \frac{dN_{\mu\mu}^-}{dE_\mu^t d\cos\theta_\mu^t} &= T \times N_D \int \frac{d\sigma_{\nu\mu}}{dE_\mu^t d\cos\theta_\mu^t} \times \frac{d^2\Phi_\mu}{dE_\nu d\cos\theta_\nu} dE_\nu d\cos\theta_\nu, \\ \frac{dN_{e\mu}^-}{dE_\mu^t d\cos\theta_\mu^t} &= T \times N_D \int \frac{d\sigma_{\nu\mu}}{dE_\mu^t d\cos\theta_\mu^t} \times \frac{d^2\Phi_e}{dE_\nu d\cos\theta_\nu} dE_\nu d\cos\theta_\nu, \end{aligned} \quad (7)$$

where  $T$  is the exposure time and  $N_D$  is the total number of target nucleons (mostly from iron) in the detector, while  $\Phi_\mu$  and  $\Phi_e$  are the atmospheric fluxes of  $\nu_\mu$  and  $\nu_e$  respectively. The label ‘ $t$ ’ refers to the true values of energy and zenith angle.

The muon energy and angle were then smeared according to the resolutions and efficiencies obtained in section 3.1 so that the event was binned according to its smeared/observed energy and angle values. Neutrino oscillation is then applied as follows.

The set of input neutrino oscillation parameters used in the analysis is listed in Table 1. Since the analysis is not sensitive to the 1–2 parameters, these were kept fixed throughout. In addition, these events are not sensitive to the CP phase, which was also kept fixed. The normal ordering was assumed to be the true one as well.

Parameter	Central/input values	$3\sigma$ ranges
$\Delta m_{21}^2$ (eV <sup>2</sup> )	$7.5 \times 10^{-5}$	fixed
$\Delta m_{32}^2$ (eV <sup>2</sup> )	$2.4 \times 10^{-3}$ (NH)	$[2.1, 2.6] \times 10^{-3}$ (NH)
$\sin^2 \theta_{12}$	0.304	fixed
$\sin^2 \theta_{23}$	0.5	[0.360, 0.659]
$\sin^2 \theta_{13}$	0.022	[0.018, 0.028]
$\delta_{CP}$ ( $^\circ$ )	0	fixed

Table 1: Values of neutrino oscillation parameters used in this study [47]. The second column shows the central values of the oscillation parameters while the third column shows the  $3\sigma$  ranges of the parameters. Normal hierarchy (NH) is assumed throughout.

Due to the presence of both  $\nu_e$  and  $\nu_\mu$  atmospheric fluxes, there are contributions from two channels, viz., the survived  $\nu_\mu$  neutrinos, determined by  $P_{\mu\mu}$  and the oscillated  $\nu_e$  neutrinos, determined by  $P_{e\mu}$ , to the muon events in ICAL. Hence each event in set I is oscillated according to  $P_{\mu\mu}(E_\nu, \cos \theta_\nu)$  as determined by the above set of oscillation parameters, while each event in set II is oscillated according to  $P_{e\mu}(E_\nu, \cos \theta_\nu)$ .

To implement oscillations we have used a re-weighting algorithm as follows. We generated a uniform random number  $r$  between 0 and 1; if  $P_{\mu\mu} > r$ , then the event survives oscillations and is binned appropriately; similarly, if  $P_{e\mu} > r$  we considered the swapped event to contribute as an oscillated  $\nu_e \rightarrow \nu_\mu$  event. Events from both channels were added to get the total  $\mu^-$  events. Symbolically, we have

$$N_\mu^- = P_{\mu\mu} N_{\mu\mu}^- + P_{e\mu} N_{e\mu}^- . \quad (8)$$

A similar procedure was applied to get  $\mu^+$  events from  $\bar{\nu}$ , with the corresponding anti-neutrino survival/oscillation probabilities.

Note that  $P_{e\mu} \ll P_{\mu\mu}$ , as can be seen from Fig. 7 where the relevant survival and oscillation probabilities for both neutrinos and anti-neutrinos have been plotted for two different values of the zenith angle,  $\cos \theta = 0.5, 1$ .

The oscillated data was binned into bins of observed/smeared muon energy and  $\cos \theta$  bins. We have used two schemes of binning in this paper. Firstly, since there were substantial events with energy  $E_\mu \gtrsim 100$  GeV, we took 25 bins of smeared energy as given in Table 2; we refer to this as exponential binning. The energy bins were optimised such as to obtain reasonable number

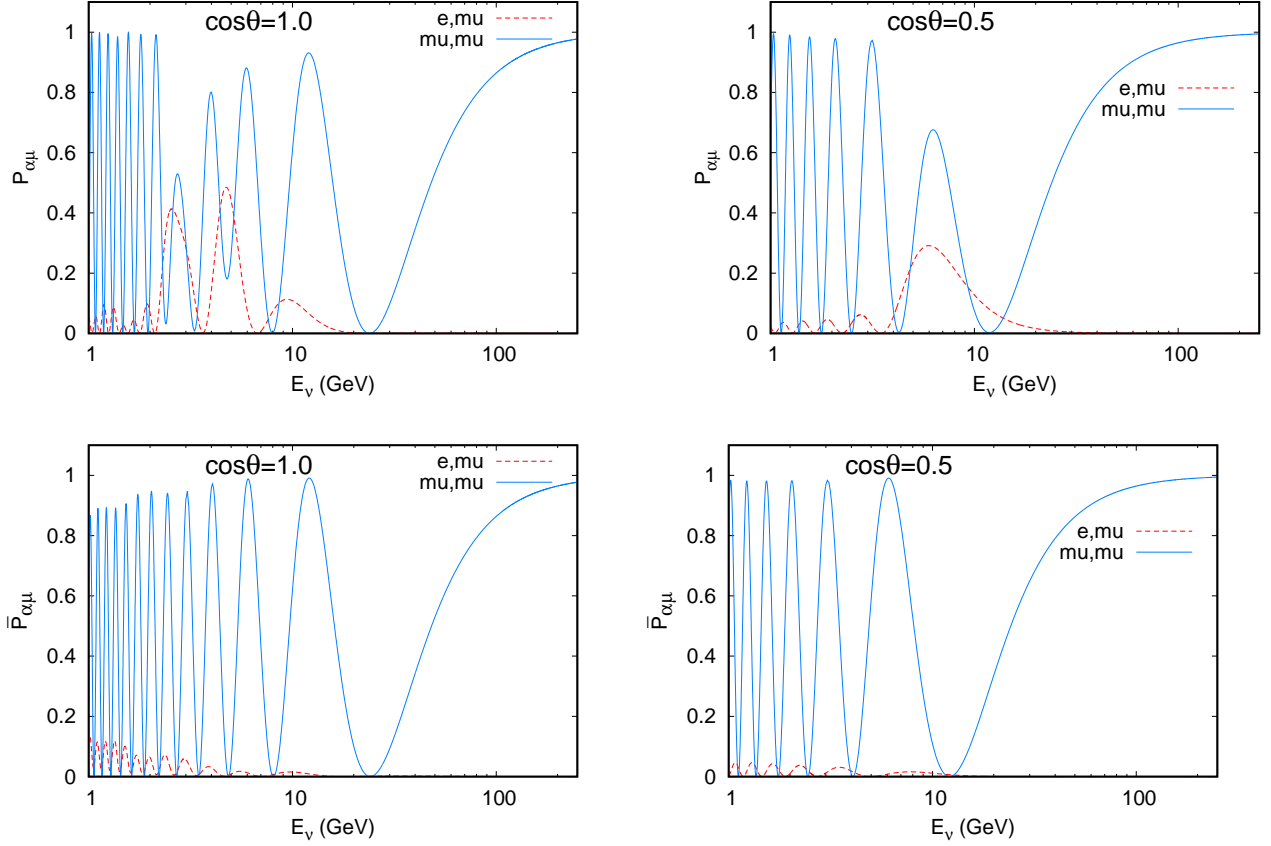


Figure 7: The survival and oscillation probabilities,  $P_{\alpha\mu}$  and  $\bar{P}_{\alpha\mu}$  for  $\alpha = e, \mu$  as a function of the neutrino energy for two different zenith angles,  $\cos\theta = 1.0, 0.5$ .

of events in each bin. Secondly, we took linear energy bins with the width of 1 GeV from 1–45 GeV. The data sample had a proportionately larger component of higher energy events which were not sensitive to oscillations, so finer bins were used at lower energy. In each case, the data was divided into seven bins of  $\cos\theta$  from 0 to 1; 6 uniform ones of width 0.15, with the last bin from 0.9–1.0.

The number of  $\mu^\pm$  events observed in a given bin  $(i, j)$  of observed  $(E_\mu^i, \cos\theta_\mu^j)$  after oscillations, and on including the detector response (smearing of muon energy and angle as well as including reconstruction and cid efficiencies) is then given by,

$$\begin{aligned} N_\mu^-(i, j) &= \epsilon_R \times [\epsilon_C^- \times N_\mu^-(E_\mu^i, \cos\theta_\mu^j) + (1 - \epsilon_C^-) \times N_\mu^+(E_\mu^i, \cos\theta_\mu^j)] , \\ N_\mu^+(i, j) &= \epsilon_R \times [\epsilon_C^+ \times N_\mu^+(E_\mu^i, \cos\theta_\mu^j) + (1 - \epsilon_C^+) \times N_\mu^-(E_\mu^i, \cos\theta_\mu^j)] , \end{aligned} \quad (9)$$

where  $N_\mu^\pm$  are the total number of  $\mu^\pm$  events in the  $(i, j)^{th}$  bin after detector smearing and oscillations,  $\epsilon_C^\pm$  is the cid efficiency (here  $\epsilon_C^+ = \epsilon_C^-$ ), and  $\epsilon_R$  is the reconstruction efficiency (which is the same for  $\mu^\pm$ ). Note that  $\epsilon_R$  and  $\epsilon_C$  have been determined from simulations as functions of the true energy and angle  $(E_\mu^t, \cos\theta^t)$  of the muons, while  $N_\mu^\pm(E_\mu, \cos\theta_\mu)$  refer to the smeared

Energy range (GeV)	Bin width (GeV)	No. of bins
1–9	1	8
9–17	2	4
17–20	3	1
20–40	5	4
40–80	10	4
80–100	20	1
100–200	50	2
200–256	56	1

Table 2: Choice of observed/smeared energy bins of muons for the case of exponential binning.

(or, in the actual experiment, observed) values for the muons. The second term in Eq. 9 is due to the charge mis-identification, and the oscillated events themselves can be obtained from the expressions given in Eqs. 7 and 8. The events oscillated according to the input parameters mentioned earlier have been scaled down to 4.5 or 10 years and labelled as “data”. The same set was scaled but oscillated according to an arbitrary set of oscillation parameters and referred to as “theory” in this simulation analysis.

The energy distribution of muons ( $E_\mu$ ) for different  $\cos\theta$  bins is shown in Fig. 8. The events fall with increasing energy. Note that the “oscillating” nature of the distribution is due to the fact that the bin sizes are not uniform; see Table 2 and associated discussion.

Events at higher energies beyond about 20 GeV are not sensitive to oscillations; however, they cannot be neglected despite being small in number as they also contribute to the statistics and help in flux normalisation since the higher energy cross sections are known better. There are just a few events in the first  $\cos\theta$  bin i.e., 0.0–0.15, reflecting the poorer resolutions and reconstruction efficiencies at large angles, as seen in Figs. 5 and 6.

## 4.2 Best fit Analysis

A  $\chi^2$  analysis has been done, taking into account systematic uncertainties through the pulls method. The  $\chi^2$  analysis uses the “data” binned in the observed momentum and zenith angle of the muons, with the addition of systematic uncertainties [48].

Five different sets of systematic uncertainties [48] were considered for our analysis as in Ref. [49]: a flux normalisation error of 20%, 10% error on cross-sections, 5% error on zenith angle dependence of flux, and an energy dependent tilt error, which is described as follows. The event spectrum have been calculated with the predicted atmospheric neutrino fluxes and with the flux spectrum shifted as,

$$\Phi_\delta(E) = \Phi_0(E) \left( \frac{E}{E_0} \right)^\delta \simeq \Phi_0(E) \left( 1 + \delta \ln \frac{E}{E_0} \right). \quad (10)$$

The different parameters are,  $E_0 = 2$  GeV,  $\delta = 1\sigma$  systematic tilt error, which was taken as 5%. In addition, an overall systematic of 5% was taken to account for uncertainties such as those

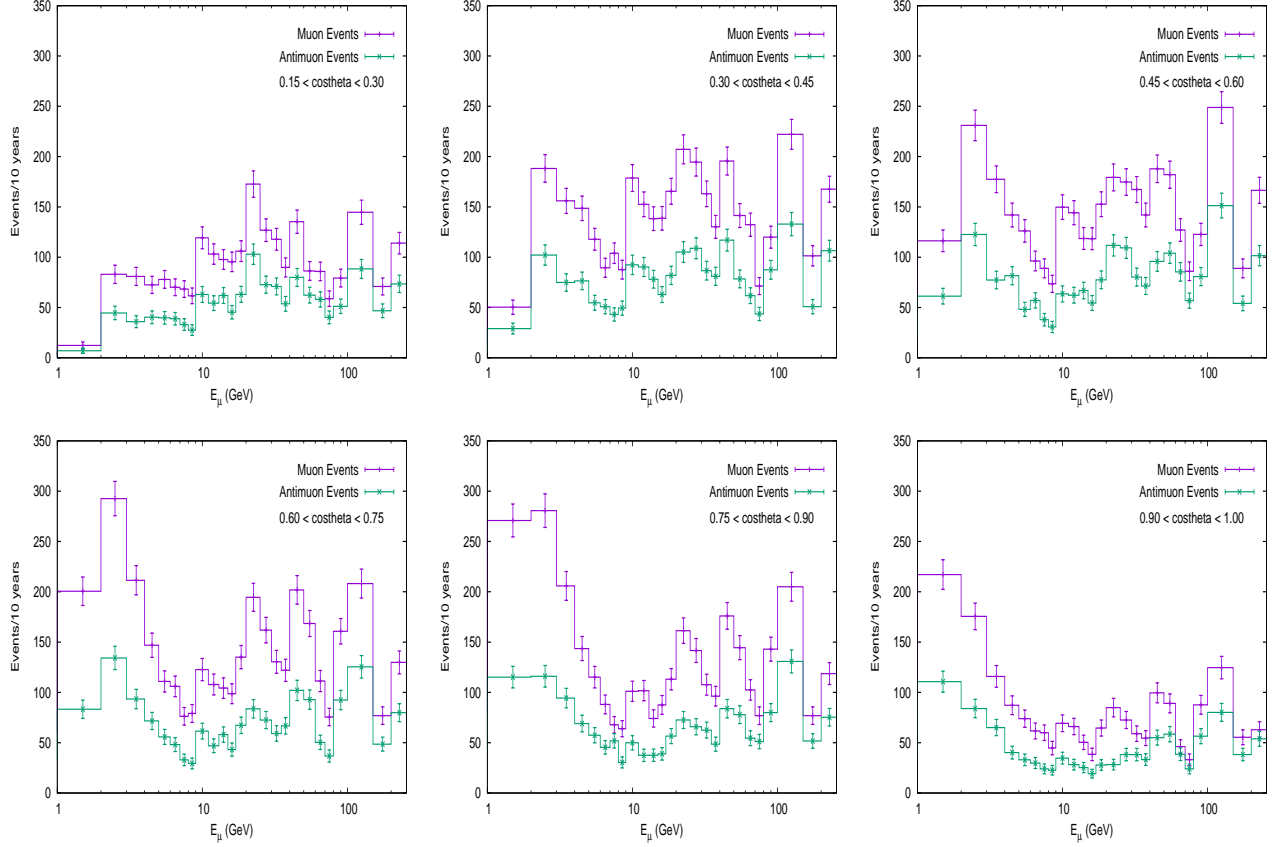


Fig. 8: Events in 10 years as a function of smeared/observed energy  $E_\mu$  for both  $\mu^-$  and  $\mu^+$  for six of the seven  $\cos\theta$  bins, excluding the most horizontal one. The central values of oscillation parameters as given in Table 1 have been used.

arising from the reconstruction of the muon energy and direction, due to uncertainties in the magnetic field used in the Kalman filter [50]. Two different analyses were performed, one where the  $\mu^+$  and  $\mu^-$  events were separately considered, and the other where they were combined into the same bins (charge-blind analysis). The former uses 10 pulls, 5 for each charge sign, while the latter uses 5 (common) pulls. Since the events in each bin are small, we use the Poissonian definition of  $\chi^2$  [51]:

$$\begin{aligned}\chi_{\pm}^2 &= \sum_{i=1, j=1} \left[ 2 \left( N_{\mu}^{\pm, \text{th}}(i, j) - N_{\mu}^{\pm, \text{obs}}(i, j) \right) - 2 N_{\mu}^{\pm, \text{obs}}(i, j) \ln \left( \frac{N_{\mu}^{\pm, \text{th}}(i, j)}{N_{\mu}^{\pm, \text{obs}}(i, j)} \right) \right] + \sum_{k=1}^5 (\xi_k^{\pm})^2 ; \\ \chi^2 &= \chi_-^2 + \chi_+^2 .\end{aligned}\tag{11}$$

Here,

$$N_{\mu}^{\pm, \text{th}}(i, j) = N_{\mu}^{\pm}(i, j) \left( 1 + \sum_{k=1}^5 \pi_{ij}^k \xi_k^{\pm} \right) ,\tag{12}$$

where  $N_{ij}^{\text{th}}$ ,  $N_{ij}^{\text{obs}}$  are the theoretically predicted data and observed data in given bins of  $(E_{\mu}, \cos \theta)$ , and  $N_{\mu}^{\pm}(i, j)$  are the number of events without the systematic uncertainties defined in Eq. 9. Here  $\pi_{ij}^k$  are the common systematic errors for  $\mu^-$  and  $\mu^+$  events, and  $\xi_k$  are the pull variables. The  $\chi_{\pm}^2$  minimisation has been done independently, first over the pulls for a given set of oscillation parameters, and then over the oscillation parameters themselves. In the analysis where the charge of the muon was not determined, the total muon events,  $N_{\mu} = (N_{\mu}^- + N_{\mu}^+)$ , were binned into the same observed  $(E_{\mu}, \cos \theta)$  bin and a common pull was applied to the summed events:

$$\chi_{\text{sum}}^2 = \sum_{i=1, j=1} \left[ 2 \left( N_{\mu}^{\text{th}}(i, j) - N_{\mu}^{\text{obs}}(i, j) \right) - 2 N_{\mu}^{\text{obs}}(i, j) \ln \left( \frac{N_{\mu}^{\text{th}}(i, j)}{N_{\mu}^{\text{obs}}(i, j)} \right) \right] + \sum_{k=1}^5 (\xi_k)^2 ;$$

where

$$N_{\mu}^{\text{th}}(i, j) = N_{\mu}^{-, \text{th}}(i, j) + N_{\mu}^{+, \text{th}}(i, j) ,\tag{13}$$

and only 5 pulls were used in the analysis.

Finally, the whole data was marginalised over the  $3\sigma$  ranges of  $\sin^2 \theta_{23}$ ,  $\Delta m_{32}^2$  and  $\theta_{13}$  given in Table 1 and a prior included on  $\sin^2 2\theta_{13}$ , as given by,

$$\chi^2 = \chi^2 + \left( \frac{\sin^2 2\theta_{13}(\text{true}) - \sin^2 2\theta_{13}}{\sigma_{\sin^2 2\theta_{13}}} \right)^2 ,\tag{14}$$

where  $\sigma_{\sin^2 2\theta_{13}}$  is the  $1\sigma$  error for the corresponding neutrino parameter which has been taken to be 8% in this analysis.

In order to determine  $\chi_{\text{min}}^2$ , the minimization of  $\chi^2$  has been done over all three parameters  $\sin^2 \theta_{23}$ ,  $\Delta m_{32}^2$  and  $\theta_{13}$ , keeping the other parameters fixed at their input values. In order to



determine the sensitivity of rock muon events to a given neutrino oscillation parameter, the change in  $\chi^2$ ,

$$\Delta\chi^2 = \chi^2(\text{par}) - \chi^2(\text{in}) , \quad (15)$$

when the “theory” events are generated using the input (in) value of the parameter, and when they are generated using a different value (par), is determined. More than one parameter can be changed in the study.

## 5 Results

### 5.1 Sensitivity to Individual Parameters

Fig. 9 shows  $\Delta\chi^2$  as a function of  $|\Delta m_{32}^2|$  using input values of  $\Delta m_{32}^2$  (true) =  $2.4 \times 10^{-3} \text{ eV}^2$  and  $\sin^2 \theta_{23} = 0.50$  with  $N_\mu^+$  and  $N_\mu^-$  events considered together and separately. It can be seen that the analysis with charge identification (cid) efficiency included (that is, separating  $N_\mu^+$  and  $N_\mu^-$  events) gives a better sensitivity than with combined events. Fig. 9 also shows a similar plot for  $\Delta\chi^2$  as a function of  $\sin^2 \theta_{23}$ , with similar improvement in the cid-dependent analysis. In both cases, the exponential energy binning scheme of Table 2 was used. Henceforth, we shall include charge identification in the analysis.

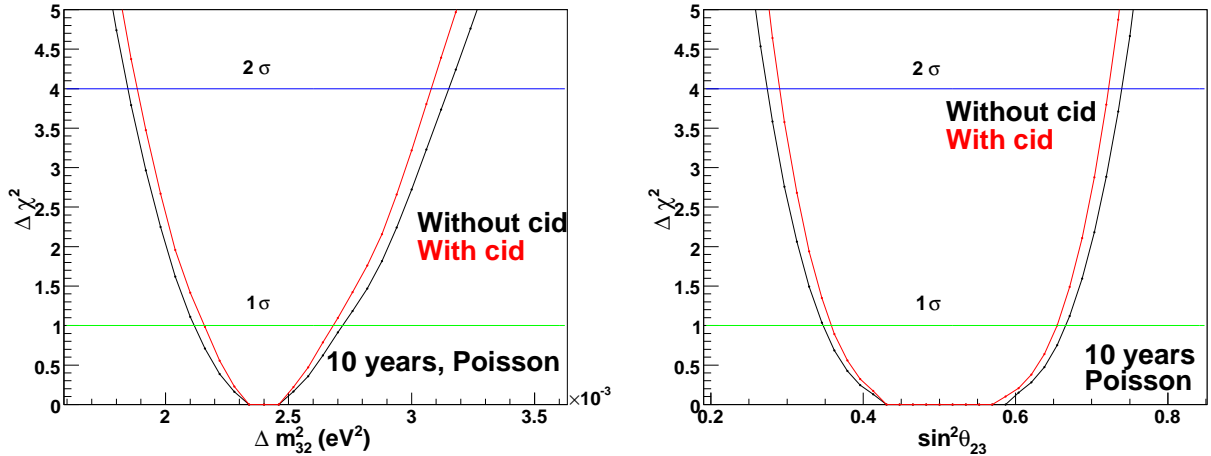


Fig. 9: A comparison of the sensitivity in  $\Delta\chi^2$  with combined muon events (without cid) (black) with an analysis including muon charge identification (with cid) with 10 systematic errors (red) as a function of  $\Delta m_{32}^2$  (left) and  $\sin^2 \theta_{23}$  (right) when their input values were taken to be  $|\Delta m_{32}^2|$  (in) =  $2.4 \times 10^{-3} \text{ eV}^2$  and  $\sin^2 \theta_{23}^{\text{in}} = 0.50$ .

Fig. 10 shows a comparison of the sensitivities when two different energy binning schemes are used (and the  $\mu^+$  and  $\mu^-$  events were separately binned). It is observed that the choice of linear energy bins improves the overall sensitivity. This is because the finer binning at lower energy in the linear bins allowed to better probe the oscillation signatures.

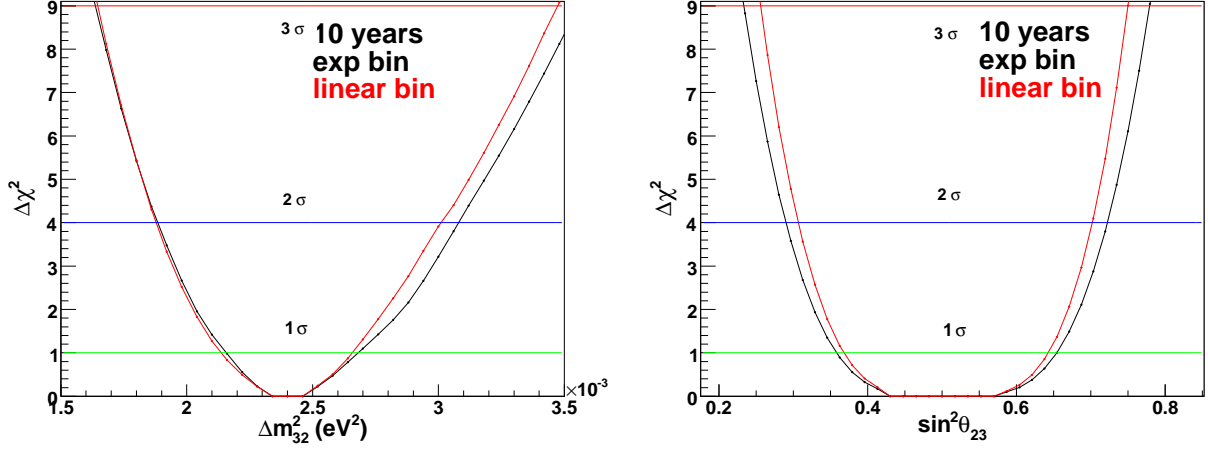


Fig. 10: A comparison of the sensitivity in  $\Delta\chi^2$  with linear binning (red) and exponential binning (black) as a function of  $\Delta m_{32}^2$  (left) and  $\sin^2 \theta_{23}$  (right) when their input values were taken to be  $|\Delta m_{32}^2|$  (in) =  $2.4 \times 10^{-3}$  eV<sup>2</sup> and  $\sin^2 \theta_{23}^{\text{in}} = 0.50$  and charge identification has been included.

## 5.2 Precision Measurements

The precision on the oscillation parameters is given by:

$$\text{Precision}^{n\sigma} = \frac{(P_{\max}^{n\sigma} - P_{\min}^{n\sigma})}{(P_{\max}^{n\sigma} + P_{\min}^{n\sigma})}, \quad (16)$$

where  $P_{\max}^{n\sigma}$  and  $P_{\min}^{n\sigma}$  are the maximum and minimum values of the concerned oscillation parameters at a given confidence level. From Tables 3, 4 we conclude that the analysis with charge separation of the muon event significantly improved the capability of ICAL detector for the estimation of oscillation parameters. In particular, the  $1\sigma$  sensitivity for  $\sin^2 \theta_{23}$  ( $\Delta m_{32}^2$ ) improved from 30% to 27% (11.5% to 10%) on changing from exponential to linear bins and including charge identification capability for the muons.

Confidence level	Precision with exponential bins		Precision with linear bins	
	Without cid (%)	With cid (%)	Without cid (%)	With cid (%)
$1\sigma$	32.0	30.0	29.5	27.0
$2\sigma$	46.0	43.0	43.0	39.0
$3\sigma$	57.0	53.0	52.5	48.0

Table 3: ICAL's capability and precision reach for measuring the atmospheric mixing angle  $\sin^2 \theta_{23}$  with a precision of at  $1\sigma$ ,  $2\sigma$  and  $3\sigma$  confidence levels respectively for both the binning schemes.

Confidence level	Precision with exponential bins		Precision with linear bins	
	Without cid (%)	With cid (%)	Without cid (%)	With cid (%)
$1\sigma$	12.7	11.5	11.3	10.0
$2\sigma$	26.5	25.4	24.2	23.3
$3\sigma$	42.4	41.3	39.3	38.3

Table 4: ICAL’s capability and precision reach for measuring the atmospheric mass squared difference  $\Delta m_{32}^2$  with a precision of at  $1\sigma$ ,  $2\sigma$  and  $3\sigma$  confidence levels respectively for both the binning schemes.

### 5.3 Allowed region in $\Delta m_{32}^2$ – $\sin^2 \theta_{23}$ parameter space

The two dimensional confidence region for the two oscillation parameters ( $\Delta m_{32}^2$ ,  $\sin^2 \theta_{23}$ ) has been determined by allowing  $\Delta m_{32}^2$ ,  $\sin^2 \theta_{23}$  and  $\sin^2 \theta_{13}$  to vary over their  $3\sigma$  ranges as shown in Table 1. The contour plots have been obtained for  $\Delta\chi^2 = \chi_{min}^2 + A$ , where  $\chi_{min}^2$  is the minimum value of  $\chi^2$  for each set of oscillation parameters and values of A are taken as 2.30, 4.61 and 9.21 corresponding to 68%, 90% and 99% confidence levels respectively for two degrees of freedom.

We have used the systematic uncertainties as described earlier and the definition of  $\chi^2$  given in Eqs. 12 and 14. In Fig. 11, the 90% CL contour of ICAL for 4.5 years data simulation (exponential binning scheme and combined  $\mu^+$  and  $\mu^-$  events) is compared with Super-Kamiokande data [30]. For Super-Kamiokande, the 90% CL allowed region of parameter space is given by ( $\sin^2 2\theta_{23} \geq 0.765$ ,  $\Delta m_{32}^2 = (1.2\text{--}4.3) \times 10^{-3} \text{ eV}^2$ ). For ICAL, the corresponding allowed region is ( $\sin^2 2\theta_{23} \geq 0.771$ ,  $\Delta m_{32}^2 = (1.48\text{--}3.7) \times 10^{-3} \text{ eV}^2$ ), so ICAL has similar sensitivity as Super-Kamiokande for the same exposure.

The precision reach expected at ICAL in the  $\sin^2 \theta_{23}$ – $\Delta m_{32}^2$  plane for 4.5-years with the exposure of 51 kt detector using two different energy binning schemes as mentioned in Section 4.1 is also shown in Fig. 11. Again, the linear binning scheme is more sensitive than the exponential one.

Fig. 12 shows the precision reach expected at ICAL in the  $\sin^2 \theta_{23}$ – $\Delta m_{32}^2$  plane for 10-years with the exposure of 51 kton detector, with and without charge identification for the exponential binning scheme. It is seen that the sensitivity improves with the addition of charge identification efficiencies in both  $\Delta m_{32}^2$  and  $\sin^2 \theta_{23}$ .

In summary, it is seen that although the muons lose different amounts of energy depending on the distance traversed in the rock, these events are still sensitive to the neutrino oscillation parameters. Due to the statistical limitations, these events do not have significant sensitivity to the sign of the 2–3 mass squared difference (sign of  $\Delta m_{32}^2$ ) or to the octant of  $\theta_{23}$  (whether this lies in the first or second quadrant, or is in fact maximal). Although the sensitivity is not as significant as that from direct detection of atmospheric neutrinos in the detector, with such low counting experiments, every independent source of information needs to be taken into account. Hence rock muon events provide a useful and independent additional source of information on the neutrino oscillation parameters in the 2–3 sector.

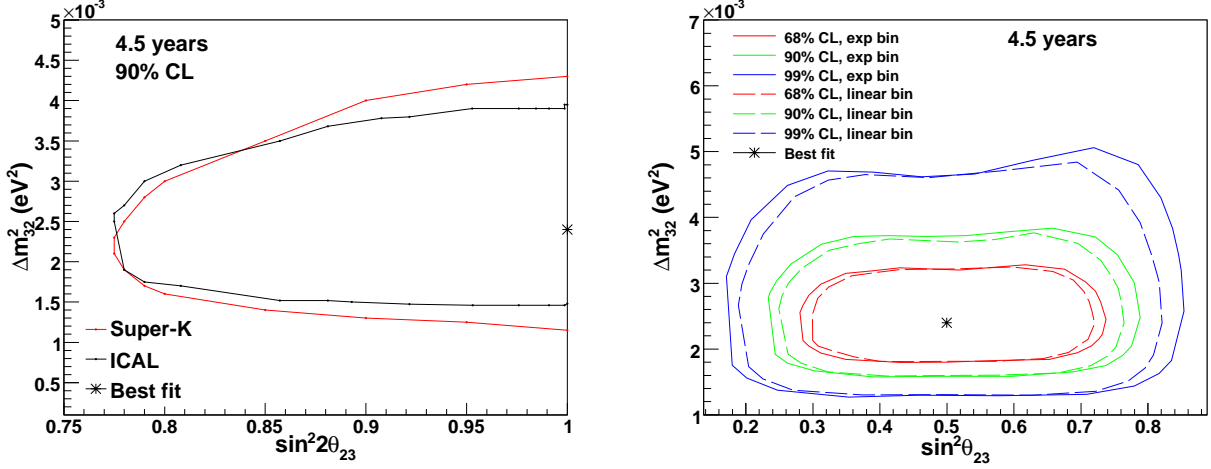


Fig. 11: The 90 % CL contour of ICAL for 4.5 years of simulated data (left) in comparison with Super-Kamiokande data [30]. The precision reach expected at ICAL in the  $\sin^2 \theta_{23}$ – $\Delta m^2_{32}$  plane for 4.5-years running of the 51 kton detector using two different energy binning schemes, viz., exponential and linear, without charge separation, is shown on the right.

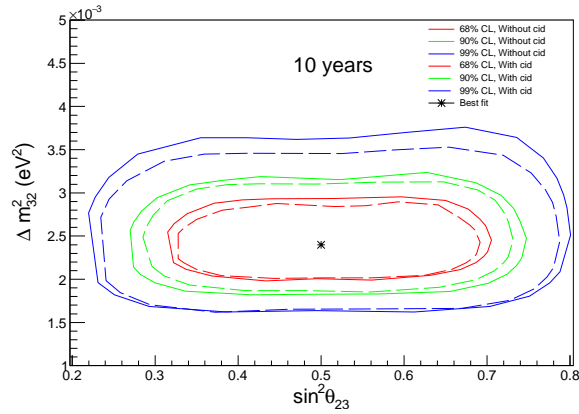


Fig. 12: The precision reach expected at ICAL in the  $\sin^2 \theta_{23}$ – $\Delta m^2_{32}$  plane for 10-years with 51 kton detector, with and without charge identification for the exponential binning scheme.

## 6 Discussions and Conclusion

A Monte Carlo simulation using the NUANCE neutrino generator for 4.5 and 10 years exposure of ICAL detector to upward-going muons, generated by the interaction of atmospheric neutrinos with the rock material surrounding the proposed ICAL detector, has been carried out. For this analysis, the muon energy and angle resolutions, as well as the reconstruction and charge identification efficiencies were separately studied for a sample of muons entering the bottom part of the detector, which is relevant for the present study.

The analysis has been done using three neutrino flavor mixing and by taking Earth matter effects into account with an angle cut ( $\cos\theta > 0.156$ ) taken such as to remove the cosmic ray muon background. A marginalised  $\Delta\chi^2$  analysis with finer bins at lower energy has been performed. Various systematic uncertainties have also been included in the analysis. The ICAL detector results were compared with Super-K detector for 4.5 years of data and both of them were comparable. The analysis was also done for 10 years of 51 kton exposure of INO-ICAL detector, with 10 systematic uncertainties, using charge separation of the upward-going muons.

The main aim of the proposed ICAL detector is to make precision measurements of neutrino oscillation parameters, especially the neutrino mass hierarchy studies, using atmospheric neutrinos. Upward-going muons arise from the interactions of atmospheric neutrinos with the rock material surrounding the detector, and they carry signatures of oscillation in spite of energy loss of the muon before they reach the detector. Hence an independent measurement of the oscillation parameters is provided by upward-going or rock muons [32, 33, 34], although the sensitivity of upward-going muons to the oscillation parameters is lower than contained vertex events where the muon neutrinos directly interact with the detector via charged current interactions to produce muons.

Since the atmospheric neutrino fluxes fall off rapidly with energy ( $\sim E^{-2.7}$ ), studies of conventional contained-vertex events in ICAL are dominated by low-energy events. In contrast, it is seen that the upward-going muon sample with a larger proportion of high energy events have a better probability of reaching the detector. Hence the contained-vertex and upward-going muons are complementary to each other. A combined analysis of both sets of events will therefore be useful to reduce overall errors due to flux and cross section normalisation uncertainties. This is beyond the scope of the current work.

**Acknowledgements** : We thank the INO physics group coordinators for their comments and suggestions on the results and the INO collaboration for their support and help. R.Kanishka thanks L.S. Mohan for help, and acknowledges UGC/DAE/DST (Govt. of India) for financial support.

## References

- [1] Y. Fukuda et al., (Super-Kamiokande collaboration), Phys Rev. Lett. 82, 2430 (1999); 86 5651 (2001).
- [2] SNO, Q. R. Ahmad et al., Phys. Rev. Lett. 87, 071301 (2001).

- [3] B. Aharmim et al., (SNO Collaboration) Phys. Rev. D 70, 093014, arXiv:hep-ex/0407029 (2004).
- [4] M. B. Smy et al., (Super-Kamiokande Collaboration), Phys. Rev. D 69, 011104, arXiv:hep-ex/0309011 (2004).
- [5] S. N. Ahmed et al., (SNO Collaboration), Phys. Rev. Lett. 92, 181301, arXiv:nucl-ex/0309004 (2004).
- [6] J. Yoo et al., (Super-Kamiokande Collaboration), Phys. Rev. D 68, 092002, arXiv:hep-ex/0307070 (2003).
- [7] B. T. Cleveland et al., Astrophys. J. 496, 505 (1998); Nucl. Phys. B (Proc. Suppl.) 38, 47 (1995).
- [8] W. Hampel et al., (Gallex Collaboration), Phys. Lett. B 447, 127 (1999).
- [9] J. N. Abdurashitov et al., (SAGE Collaboration), Phys. Rev. C 60, 055801 (1999).
- [10] M. Altmann et al., (GNO Collaboration), Phys. Lett. B 490, 16, arXiv:hep-ex/0006034 (2000).
- [11] Super-Kamiokande, Y. Fukuda et al., Phys. Rev. Lett. 81, 1562, arXiv:hep-ex/9807003 (1998).
- [12] Super-Kamiokande, Y. Fukuda et al., Phys. Rev. Lett. 82, 2644, arXiv:hep-ex/9812014 (1999).
- [13] Super-Kamiokande, Y. Fukuda et al., Phys. Lett. B 433, 9, arXiv:hep-ex/9803006 (1998).
- [14] Super-Kamiokande, Y. Fukuda et al., Phys. Lett. B 436, 33, arXiv:hep-ex/9805006 (1998).
- [15] Super-Kamiokande, S. Fukuda et al., Phys. Rev. Lett. 85 3999, arXiv:hep-ex/0009001 (2000).
- [16] W. W. M. Allison et al., (Soudan-2 Collaboration), Phys. Lett. B 449, 137, arXiv:hep-ex/9901024 (1999).
- [17] M. Ambrosio et al., (MACRO Collaboration), Phys. Lett. B 478, 5 (2000).
- [18] M. Ambrosio et al., (MACRO Collaboration), Phys. Lett. B 566, 35, arXiv:hep-ex/0304037 (2003).
- [19] M. Sanchez et al., (Soudan 2 Collaboration), Phys. Rev. D 68, 113004, arXiv:hep-ex/0307069 (2003).
- [20] M. H. Ahn et al., (K2K Collaboration), Phys. Rev. Lett. 90, 041801, arXiv:hep-ex/0212007 (2003).



- [21] K. Eguchi et al., (KamLAND Collaboration), Phys. Rev. Lett. 90, 021802, arXiv:hep-ex/0212021 (2003).
- [22] B. Pontecorvo, Sov. Phys. JETP 26, 984 (1968); Zh. Eksp. Teor. Fiz. 53, 1717 (1967).
- [23] Z. Maki, M. Nakagawa and S. Sakata, Prog. Theor. Phys. 28, 870 (1962).
- [24] J. K. Ahn et al., (RENO Collaboration) *Observation of Reactor Electron Antineutrino Disappearance in the RENO Experiment*, Phys. Rev. Lett. 108, 191802, arXiv:hep-ex/1204.0626 (2012).
- [25] F. P. An et al., (DAYA BAY Collaboration) *Observation of electron-antineutrino disappearance at Daya Bay*, Phys. Rev. Lett. 108, 171803, arXiv:hep-ex/1203.1669 (2012).
- [26] A. Ghosh, T. Thakore and S. Choubey, *Determining the Neutrino Mass Hierarchy with INO, T2K, NOvA and Reactor Experiments*, JHEP **1304**, 009, arXiv:hep-ph/1212.1305 (2013).
- [27] M. S. Athar et al., *India-based Neutrino Observatory: Project Report Volume I*, <http://www.ino.tifr.res.in/ino/OpenReports/INOREport.pdf> (2006).
- [28] B. Abi et al., DUNE Collaboration, *Long-baseline neutrino oscillation physics potential of the DUNE experiment*, Eur.Phys.J **C 80** (2020) 10, 978; arXiv: 2006.16043 [hep-ex].
- [29] H. Lu, for the JUNO Collaboration, *The physics potentials of JUNO*, Phys.Scripta **96** (2021) 9, 094013.
- [30] Kazunori Nitta, *Neutrino Oscillation Analysis of Upward Through-going and Stopping Muons in Super-Kamiokande*, PhD thesis, Department of Physics, Osaka University, <http://www-sk.icrr.u-tokyo.ac.jp/sk/pub/nitta.pdf> (2003).
- [31] T. Stanev, *High Energy Cosmic Rays*, Springer-Praxis, Berlin (2003).
- [32] A. Habig et al., *Measurement of the flux and zenith-angle distribution of upward through-going muons by Super-Kamiokande*, arXiv:hep-ex/9812014v2, 18 March 1999.
- [33] Y. Ashie et al., *A Measurement of Atmospheric Neutrino Oscillation Parameters by Super-Kamiokande-I*, arXiv:hep-ex/0501064v2, 15 Jun 2005.
- [34] M. Ambrosio et al., *Measurement of the atmospheric neutrino-induced upgoing muon flux using MACRO*, arXiv:hep-ex/9807005v1, 7 July 1998.
- [35] P.A. Zyla et al., *Particle Data Group*, Prog. Theor. Exp. Phys. 2020, 083C01 (2020) and 2021 update.
- [36] D. Casper, *The Nuance neutrino physics simulation, and the future*, Nucl. Phys. Proc. Suppl. **112** 161–170, [arXiv:0208030] (2002).
- [37] D. Indumathi, M. V. N. Murthy, G. Rajasekaran and N. Sinha, Phys. Rev. D 74, 053004, arXiv:hep-ph/0603264 (2006).

- [38] V. Barger, R. Gandhi, P. Ghoshal, S. Goswami, D. Marfatia, S. Prakash, S. K. Raut and S. U. Sankar, Phys. Rev. Lett. 109, 091801, arXiv:hep-ph/1203.6012 (2012).
- [39] B. Satyanarayana, *Design and Characterisation Studies of Resistive Plate Chambers*, Ph.D thesis, Department of Physics, IIT Bombay, PHY-PHD-10-701, (2009).
- [40] M. M. Devi et al., *Hadron energy response of the Iron Calorimeter detector at the India-based Neutrino Observatory*, JINST **8** P11003, [arXiv:1304.5115] (2013).
- [41] Infolytica Corp., *Electromagnetic field simulation software*, <http://www.infolytica.com/en/products/magnet/>.
- [42] A. Chatterjee et al., *A Simulations Study of the Muon Response of the Iron Calorimeter detector at the India-based Neutrino Observatory*, JINST **9** P07001, [arXiv:1405.7243] (2014).
- [43] R. Kanishka et al., *Simulations study of muon response in the peripheral regions of the Iron Calorimeter detector at the India-based Neutrino Observatory*, JINST **10** P03011, [arXiv:1503.03369] (2015).
- [44] M. Honda T. Kajita, K. Kasahara and S. Midorikawa, Phys. Rev. D 70, 043008, arXiv:astro-ph/0404457 (2004).
- [45] Y. Ashie et al., (Super-Kamiokande Collaboration), Phys. Rev. Lett. 93, 101801, arXiv:hep-ex/0404034v1 (2004).
- [46] Kanishka, *A Study of upward-going muons in ICAL detector at India-based neutrino observatory*, Ph.D. Thesis, Department of Physics, Panjab University Chandigarh (2015).
- [47] Mohan L. S., Indumathi D., *Pinning down neutrino oscillation parameters in the 2-3 sector with a magnetised atmospheric neutrino detector: a new study*. Eur. Phys. J. C 77, 54, <https://doi.org/10.1140/epjc/s10052-017-4608-0> (2017).
- [48] Michele Maltoni, M.C. Gonzalez-Garcia et. al., *Atmospheric neutrino Oscillations and new Physics* Phys. Rev. D 70, 033010, arXiv:hep-ph/0404085v1 (2004).
- [49] Lakshmi S Mohan, *Precision measurement of neutrino oscillation parameters at INO ICAL*, Ph.D. Thesis, Homi Bhabha National Institute (HBNI) (2015).
- [50] Kolahal Bhattacharya, et al., (INO Collaboration), *Error propagation of the track model and track fitting strategy for the iron calorimeter detector in India-based neutrino observatory*, Computer Physics Communications (Elsevier) **185** (12) 3259–3268, (2014).
- [51] T. Thakore, A. Ghosh, S. Choubey and A. Dighe, *The Reach of INO for Atmospheric Neutrino Oscillation Parameters*, JHEP **1305**, 058, arXiv:hep-ph/1303.2534 (2013).